*photonics*

MDPI

*Article*

# Polarization-Guided Blind Unmixing for Multi-Target Scattering Imaging Beyond the Optical Memory Effect

**Jingbo Duan [1], Tong Zhang [1,*], Xue Dong [1], Pingli Han [1] and Fei Liu [1,2]**

[1] School of Optoelectronic Engineering, Xidian Univeristy, Xi'an 710071, China; 21051110095@stu.xidian.edu.cn (J.D.); xuedong@xidian.edu.cn (X.D.); plhan@xidian.edu.cn (P.H.); feiliu@xidian.edu.cn (F.L.)

[2] State Key Laboratory of Electromechanical Integrated Manufacturing of High-Performance Electronic Equipment, Xi'an 710071, China

* Correspondence: zhangtong01@xidian.edu.cn

**Abstract**

Multi-target imaging beyond the optical memory effect (OME) is fundamentally challenged by the incoherent superposition of speckles originating from different OME regions, which renders object separation highly ill-posed. To address this challenge, we introduce a polarization-guided blind unmixing framework that exploits the distinct polarization responses of different targets as an additional discrimination cue for speckle separation. Polarized speckles are first used to construct a dense polarization-response representation through Stokes-based synthesis. The resulting polarization diversity is leveraged to estimate the number of targets without prior knowledge and to identify structurally representative autocorrelation endmembers associated with different objects. An energy-constrained non-negative matrix factorization is then developed to separate individual target autocorrelations, followed by phase retrieval for object reconstruction. Experimental results demonstrate the reconstruction of up to five targets located beyond the OME range, achieving target separations of up to 2.6× the measured OME limit and peak signal-to-noise ratio (PSNR) values above 25 dB, without requiring prior knowledge of target locations, structures, polarization states, or target number.

**Keywords:** scattering imaging; optical memory effect; multi-target separation; polarization measurement; speckle correlation imaging

## 1. Introduction

Optical imaging techniques traditionally rely on the principle that light propagates rectilinearly in homogeneous media [1–3]. Scattering media, including clouds, turbid liquids, and biological tissues, induce multiple scattering that randomizes propagation trajectories and precludes direct imaging with conventional approaches. Established methods for imaging through scattering media include wavefront shaping, transmission matrix characterization [4–9], invasive point-spread-function (PSF) deconvolution [10], and speckle correlation imaging (SCI) [11]. Among these, SCI is notable for its non-invasive nature and single-shot acquisition capability, making it particularly promising for real-time applications. However, the field of view (FOV) of SCI is fundamentally limited by the angular extent of the optical memory effect (OME), which restricts its utility in wide-field imaging scenarios [12,13].

Research on achieving large-field-of-view imaging beyond the OME in scattering media can be grouped into several main strategies. One prominent approach employs

Check for updates

Received: 26 June 2026
Revised: 9 July 2026
Accepted: 14 July 2026
Published: 16 July 2026

spatial demultiplexing techniques that leverage prior information, such as a pre-collected point spread function (PSF) [14], known target positions [15], or prior knowledge of the number of objects [16]. While these methods can indeed extend imaging beyond the OME range, their reliance on invasive measurements and cumbersome calibration procedures severely hampers their practicality in dynamic or inaccessible environments. A second class of methods establishes a rigorous mathematical relationship between the input optical field and the output speckle field by measuring the transmission matrix of the scattering medium [17]. Although these approaches can effectively extend the OME for imaging through stable media, they incur prohibitively high computational costs and are sensitive to system perturbations. In parallel, neural-network-based approaches have been trained to learn the statistical correlation between hidden targets and their resultant speckle patterns, enabling the decoding of target structures from aliased speckles for exceed-OME imaging [18–24]. Despite their promise, these data-driven methods demand large-scale training datasets and lengthy training periods, and their computational complexity often precludes real-time or high-speed imaging applications.

A fundamentally different approach to circumvent the OME limitation arises from the observation that speckles originating from multiple targets separated beyond the OME range are mutually uncorrelated. Under this condition, the composite speckle pattern recorded by the camera is approximately the linear superposition of the individual speckle intensities generated by each target. This linear superposition property enables spatially resolved target reconstruction across large FOVs by disentangling overlapping speckle patterns. Building upon this principle, Wei et al. [25] developed a method for imaging two isolated objects through a thin scattering medium, achieving simultaneous improvement in both field of view and depth of field. However, their approach relies on relative motion between two objects, with one target moving around the other position-fixed object, which imposes stringent constraints on the imaging scenario and limits its broader applicability. Subsequently, Wang et al. [26] proposed a prior-information-free single-shot scattering imaging method to exceed the ME range, separating the autocorrelation of each target from the recorded dual-target speckle via Fourier spectrum guessing and iterative energy-constrained compensation. Nevertheless, this method is specifically designed for dual-target scenarios and requires that the two targets possess nearly identical luminous flux to ensure successful separation, which significantly restricts its practical deployment. Li et al. [27] introduced a more general framework combining light emphasis modulation with independent component analysis for speckle separation, demonstrating the capability to handle multi-target scenes beyond the OME range for the first time. However, their approach still requires multiple sequential acquisitions under different modulation conditions, precluding single-shot operation. Wang et al. [28] further advanced this line of work by developing a blind target position detection method for large-field-of-view scattering imaging, employing a low-cross-talk region allocation strategy to isolate individual target autocorrelations without requiring any prior information. This method requires two captured speckles at different imaging distances and involves solving complex inverse problems, with computational cost growing significantly as the number of targets increases. More recently, Zhu et al. [29] proposed a prior-free mixed speckle simplex separation strategy based on non-negative matrix factorization, achieving multi-object imaging beyond at least four times the OME range. Despite these advances, a common and fundamental limitation of all existing methods in this category is their requirement for multiple speckle acquisitions (temporal, spatial, or modulation-domain multiplexing), rendering them inapplicable in high-speed imaging scenarios where only a single-frame acquisition is available.

In addition to intensity, polarization provides an important dimension of information that can be exploited in scattering imaging. The Stokes parameters fully characterize the po-

https://doi.org/10.3390/photonics13070680

larization state of scattered light, allowing multiple independent observables to be extracted without modifying the optical setup [30–32]. Polarization diversity has been successfully applied to enhance image contrast, reduce background scattering, and separate mixed sources in complex media [33–37]. For multiple targets exhibiting distinct polarization responses, the composite speckle pattern acquired at different analyzer angles contains polarization-encoded information specific to each target. This property suggests that polarization can serve as an effective demixing domain: by exploiting the distinct polarization fingerprints of individual targets, one can separate their contributions from a single mixed speckle field without resorting to spatial or temporal multiplexing. This polarization-based demixing strategy thus provides a means to overcome the OME-imposed FOV constraint while retaining the single-shot capability required for real-time applications.

Motivated by these advances, we propose a single-shot polarization-based blind unmixing framework that jointly exploits polarization diversity and statistical decomposition to achieve multi-target imaging beyond the OME range. From four polarization-analyzed speckle images, Stokes parameters are computed and used to synthesize a set of virtual speckle patterns at multiple polarization angles, creating a redundant representation that enhances polarization-induced diversity. A log-domain non-local means filter is applied to suppress noise while amplifying weak-target features. The number of targets is estimated without prior knowledge through local peak detection and principal component analysis of polarization response vectors, circumventing the rank deficiency inherent in global Stokes-subspace analysis. Structurally distinct autocorrelation (AC) signatures are then selected as endmembers via zero-mean normalized cross-correlation, and an energy-constrained non-negative matrix factorization separates the individual target autocorrelations by incorporating the prior that each target contributes proportionally to its center-peak intensity. Phase retrieval finally reconstructs each target. It is worth noting that the proposed framework is inherently compatible with single-shot operation, as a polarization-resolving camera can capture all four polarization channels in a single exposure. In the current implementation, we use a rotating analyzer with a 16-bit camera due to the limited sensitivity of commercially available 8-bit polarization cameras under low-signal conditions. Experimental results demonstrate that the proposed method successfully recovers multiple targets located beyond the OME range from a single exposure, without requiring any prior knowledge of target positions, shapes, polarization states, or the number of targets.

## 2. Method

### 2.1. Speckle Superposition Model

The optical memory effect (OME) is a fundamental property of wave scattering that enables shift-invariant imaging through a thin scattering layer [4]. When a coherent or partially coherent light beam illuminates an object placed behind a scattering medium, the transmitted wavefront undergoes multiple scattering events, creating a seemingly random speckle pattern on the detector. Remarkably, if the incident beam direction is changed by a small angle within a specific angular range, the speckle pattern does not decorrelate completely; rather, it shifts rigidly on the detection plane with high fidelity. This angular range, within which the speckle pattern remains highly correlated and translates proportionally to the incident tilt, defines the OME region.

Within a single OME zone, the scattering medium can be effectively modeled as a linear shift-invariant system. The system's point spread function PSF, denoted by $P$, is then a stationary speckle pattern that encodes the random phase scrambling imparted by the medium. As a result, the speckle intensity distribution $I$ recorded on the sensor is simply the convolution between the object's intensity transmission $O$ and the PSF $P$:

$$I(\mathbf{r}) = \int O(\mathbf{r}')\, P(\mathbf{r} - \mathbf{r}')\, d\mathbf{r}' = O * P. \tag{1}$$

This convolution relationship forms the backbone of speckle correlation imaging (SCI): the object's Fourier magnitude can be recovered from the autocorrelation of the measured speckle, after which the lost phase is retrieved via phase retrieval algorithms, ultimately reconstructing the object's shape.

However, the OME also imposes a strict limitation on the field of view (FOV). Once the lateral extent of the object plane exceeds the OME range, the shift-invariance assumption breaks down. Suppose the object plane contains $N$ spatially separated targets $O_i(\mathbf{r})$ ($i = 1, \ldots, N$), each residing in a distinct OME domain. Because the medium responds with a different, uncorrelated PSF $P_i$ for each OME zone, the detected speckle pattern no longer originates from a single convolution. Instead, the total intensity is the linear superposition of the individual speckle fields generated by each target independently:

$$I(\mathbf{r}) = \sum_{i=1}^{N} (O_i * P_i)(\mathbf{r}) = \sum_{i=1}^{N} s_i(\mathbf{r}). \tag{2}$$

Here $s_i$ denotes the individual speckle pattern contributed by the $i$-th target, and the PSFs $P_i$ are mutually uncorrelated because they belong to different OME regions. Equation (2) describes the essential challenge of multi-target imaging beyond the OME: the recorded image is an inseparable mixture of multiple unknown speckle patterns, each carrying the structural information of one target. Recovering $\{O_i\}$ from a single mixed speckle measurement without prior knowledge of the PSFs or target locations is therefore a severely ill-posed inverse problem.

### 2.2. Polarized Unmixing Framework for Beyond-OME Imaging

To address the challenge of multi-target imaging beyond the OME range through scattering media, we introduce a polarization-domain decoding technique for mixed speckles. This method extends traditional intensity-only speckle correlation imaging by incorporating polarization as an additional degree of freedom for speckle separation. As illustrated in Figure 1a, we first describe the formation of mixed speckles on the detection plane in the polarization domain, where multiple targets exhibit distinct polarization characteristics after illumination.

Each target exhibits a specific linear polarization response characterized by a polarization angle $\theta_i$. When the effective thickness of the scattering medium is less than or roughly equal to the transport mean free path (TMFP) but longer than the scattering mean free path (SMFP), the polarization states of the optical beams can still be maintained after passing through the scattering medium [38]. Under this condition, by placing an analyzer at four angles $\omega \in \{0°, 45°, 90°, 135°\}$ in front of the camera, the acquired speckle image at each angle becomes a linear mixture of individual target speckle patterns weighted by Malus law coefficients:

$$I(\omega) = \sum_{i=1}^{N} \alpha_i(\omega) \cdot s_i \tag{3}$$

where $\alpha_i(\omega) = \cos^2(\omega - \theta_i)$ is the polarization weight of the $i$-th target, determined by its inherent polarization angle $\theta_i$.

With only four polarization channels, the mixing equation in Equation (3) constitutes an underdetermined linear system when $N > 4$. To solve this underdetermined inverse problem without increasing acquisition times, we expand the effective information dimensionality via polarization diversity (see Figure 1b–e). From the Stokes parameters computed from the four acquired images, $M = 180$ virtual speckle images are synthesized at uniformly spaced polarization angles according to the Malus law. This redundant multi-angle representation creates the necessary diversity for blind separation, as each target alternately dominates the local speckle contrast at its corresponding optimal polarization angle.

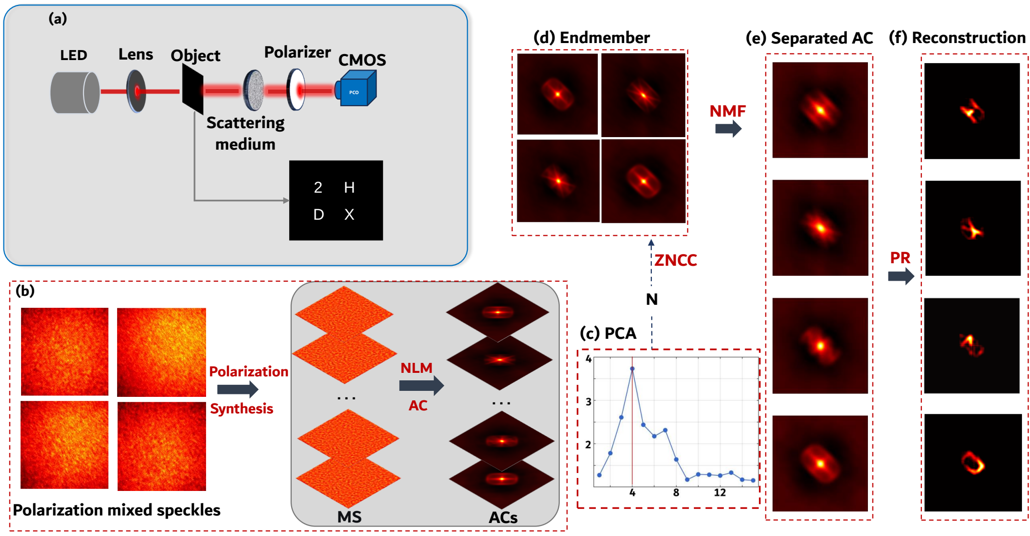


**Figure 1.** Schematic illustration of the process of the proposed method for realizing noninvasive scattering imaging of multiple targets beyond the OME. (**a**) Transmissive imaging configuration. (**b**–**f**) The data processing of the polarization demixing method. MS denotes the multi-angle synthesized speckles; ACs denotes the corresponding autocorrelations of the synthesized speckles.

The proposed method proceeds in two main stages. Before the target count is known, the virtual images are enhanced by a log-domain non-local means filter to amplify weak target regions, and local peak detection combined with principal component analysis (PCA) of polarization response vectors provides a data-driven estimate of $N$. Once $N$ is determined, structurally distinct endmember autocorrelations are selected via zero-mean normalized cross-correlation (ZNCC) analysis of the enhanced virtual images, and an energy-constrained non-negative matrix factorization (NMF) separates the individual target autocorrelations. Finally, each target is reconstructed from its separated autocorrelation via phase retrieval [39–41]. The following subsections detail each stage.

### 2.2.1. Polarization-Domain Preprocessing

The four polarization-resolved speckle images $I_0$, $I_{45}$, $I_{90}$, and $I_{135}$ first undergo background correction and Gaussian smoothing to eliminate uneven illumination and suppress camera noise. From the preprocessed images, the Stokes parameters are computed as $S_0 = I_0 + I_{90}$, $S_1 = I_0 - I_{90}$, and $S_2 = I_{45} - I_{135}$, which fully characterize the polarization state of the scattered light. For any polarization analysis angle $\alpha$, the transmitted intensity follows Malus's law, according to which the transmitted intensity of perfectly linearly polarized light passing through an ideal linear polarizer is proportional to the square of the cosine of the angle between the incident polarization direction and the transmission axis of the polarizer. This polarization transformation can be mathematically described through the Mueller matrix:

$$\begin{bmatrix} I'_p \\ Q'_p \\ U'_p \\ V'_p \end{bmatrix} = \frac{1}{2} \begin{bmatrix} 1 & \cos 2\alpha & \sin 2\alpha & 0 \\ \cos 2\alpha & \cos^2 2\alpha & \cos 2\alpha \sin 2\alpha & 0 \\ \sin 2\alpha & \cos 2\alpha \sin 2\alpha & \sin^2 2\alpha & 0 \\ 0 & 0 & 0 & 0 \end{bmatrix} \begin{bmatrix} I_p \\ Q_p \\ U_p \\ V_p \end{bmatrix}. \quad (4)$$

The intensity of the outgoing light is therefore given by the inner product of the first row of the Mueller matrix with the incident Stokes vector. For an arbitrary polarization analysis angle $\alpha$ this yields:

$$I(\alpha) = \frac{S_0 + S_1 \cos 2\alpha + S_2 \sin 2\alpha}{2}. \tag{5}$$

We uniformly sample $\alpha$ from 0° to 180° with a step of 1°, generating $M = 180$ virtual speckle images. Although all these images lie within a three-dimensional Stokes subspace, the redundant multi-angle representation enables targets with different polarization angles to alternately dominate local speckle contrast, thereby creating the diversity required for blind separation.

To amplify weak target regions that are easily overwhelmed by strong speckle fluctuations from brighter targets, we apply a log-domain non-local means (NLM) filter to each virtual image. The logarithmic transformation:

$$L = \log(I + 1) \tag{6}$$

compresses the extreme dynamic range of speckle intensities, bringing weak fluctuations closer in magnitude to strong ones. Each pixel $i$ is then denoised by a weighted average of pixels $j$ within a search window:

$$\tilde{L}_i = \frac{1}{Z_i} \sum_j w_{ij} L_j, \quad w_{ij} = \exp\left( -\frac{\|P_i - P_j\|^2}{h^2} \right) \tag{7}$$

where $P_i$ is a $5 \times 5$ patch centered at pixel $i$, $\|\cdot\|$ denotes the Euclidean distance, $h$ controls the smoothing strength, and $Z_i = \sum_j w_{ij}$ normalizes the weights.

By exploiting the self-similarity of speckle patterns, the NLM filter suppresses noise while preserving intrinsic texture structures. As illustrated in Figure 2, the log-domain NLM enhancement effectively amplifies weak-target signatures: the autocorrelation (Figure 2a,f) and the log-domain Fourier magnitude (Figure 2c,d) show much clearer peaks and improved contrast after filtering, while the enhanced speckle pattern in Figure 2e exhibits more distinguishable local structures compared with its unprocessed version in Figure 2b. This log-NLM operation enhances the local contrast of weak target regions, making them distinguishable from the background in subsequent processing. Since both the logarithmic compression and patch-based averaging are performed independently for each polarization angle, the relative structural differences among virtual images encoded by polarization modulation coefficients are fully preserved.

After enhancement, we estimate the number of targets $N$ by exploiting the spatial locality of speckle patterns. The full width at half maximum (FWHM) of the average speckle autocorrelation, denoted $w$, is first measured from the enhanced images. For each enhanced image, local intensity maxima are detected using a circular neighborhood of radius $w/2$, and the $N_p$ peaks are retained per angle. At each retained peak location $\boldsymbol{r}$, a local patch of size $w \times w$ is extracted from each of the $M$ virtual speckle images. These patches are vectorized and concatenated to form a high-dimensional polarization–spatial feature vector:

$$\boldsymbol{p} = \left[ \mathrm{vec}(\tilde{I}_1(\mathcal{N}(\boldsymbol{r})))^T, \ldots, \mathrm{vec}(\tilde{I}_M(\mathcal{N}(\boldsymbol{r})))^T \right]^T \tag{8}$$

where $\mathcal{N}(\boldsymbol{r})$ denotes the $w \times w$ local neighborhood centered at $\boldsymbol{r}$, and $\mathrm{vec}(\cdot)$ vectorizes the patch. This vector encodes both the local spatial structure of the speckle pattern and the polarization response at that location. All such vectors are centered and arranged into a matrix $\boldsymbol{P}$, and PCA is performed on $\boldsymbol{P}^T\boldsymbol{P}$. The physical basis for this localized PCA strategy is that each target produces local intensity peaks within its own speckle pattern, and the polarization–spatial feature vectors extracted at these peaks share a common fingerprint corresponding to that target. Consequently, peaks belonging to different targets form distinct clusters in the feature space. Let $\lambda_1 \geq \lambda_2 \geq \cdots$ be the eigenvalues of $\boldsymbol{P}^T\boldsymbol{P}$ sorted in descending order. The number of targets $N$ is then determined by the eigenvalue ratio criterion:

$$N = \arg\max_k \frac{\lambda_k}{\lambda_{k+1} + \varepsilon}, \quad k = 1, 2, \ldots, L \tag{9}$$

where $L$ is the total number of retained peaks, and $\varepsilon = 10^{-12}$ is a small constant introduced solely to avoid division by zero. As shown in Figure 1c, this ratio reaches its maximum at $N = 4$, which correctly indicates the number of targets in our experiment.

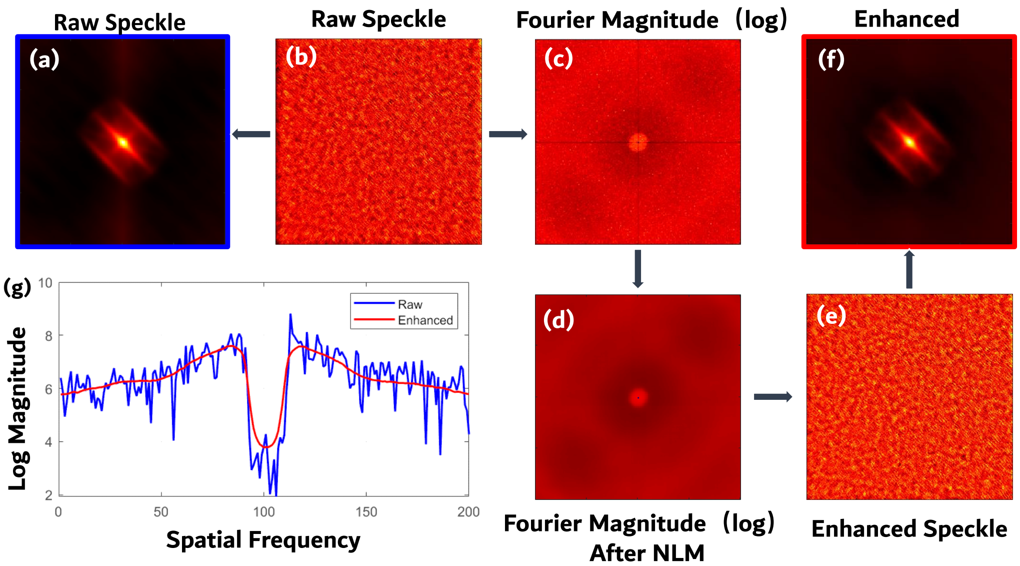


**Figure 2.** Effectiveness of the log-domain NLM enhancement. (**a**) Autocorrelation of a single-angle speckle pattern before enhancement. (**b**) The corresponding speckle pattern before enhancement. (**c**) Log-domain Fourier magnitude of the speckle shown in (**b**). (**d**) Log-domain Fourier magnitude after NLM filtering. (**e**) The speckle pattern after log-domain NLM enhancement. (**f**) Autocorrelation of the enhanced speckle shown in (**e**). (**g**) Center profiles of the log-domain Fourier magnitude before and after NLM enhancement, taken along the horizontal axis.

This localized PCA strategy breaks the global rank deficiency of the Stokes subspace, as the peak locations are scattered across different target regions and capture the distinct polarization fingerprint of each target. The log-NLM enhancement ensures that even low-intensity targets contribute detectable peaks, so that $N$ correctly accounts for all targets.

### 2.2.2. Endmember-Guided Constrained Blind Unmixing

With the number of targets $N$ determined, we proceed to select $N$ structurally representative autocorrelations from the $M$ virtual images to serve as endmembers. For each enhanced virtual speckle image $\tilde{I}_k$, its autocorrelation is computed as:

$$R_k = \mathcal{F}^{-1}\left\{ \left| \mathcal{F}\{\tilde{I}_k\} \right|^2 \right\} \tag{10}$$

where $\mathcal{F}\{\cdot\}$ and $\mathcal{F}^{-1}\{\cdot\}$ denote the Fourier transform and inverse Fourier transform, respectively. The central region of each autocorrelation is retained to focus on target-shape-related structures.

The structural similarity between any two autocorrelations $R_i$ and $R_j$ is quantified by zero-mean normalized cross-correlation:

$$\mathrm{ZNCC}(R_i, R_j) = \frac{\sum(R_i - \bar{R}_i)(R_j - \bar{R}_j)}{\sqrt{\sum(R_i - \bar{R}_i)^2 \sum(R_j - \bar{R}_j)^2}} \tag{11}$$

a metric insensitive to absolute intensity and contrast variations.

Computing ZNCC for all pairs yields an $M \times M$ similarity matrix, whose average curve $\bar{z}(\alpha)$ exhibits valleys at angles where a single target dominates. Selecting the deepest and most dispersed valleys via a max–min criterion produces $N$ endmember autocorrelations $\boldsymbol{x}_1, \ldots, \boldsymbol{x}_N$, each primarily driven by a different target.

These endmember autocorrelations are vectorized and stacked into the observation matrix $X = [\boldsymbol{x}_1, \ldots, \boldsymbol{x}_N]$. We aim to decompose $X \approx WH$ with non-negative matrices $W$ and mixing coefficients $H$. Standard NMF often fails on such data: one component absorbs the strong center peak common to all views, leaving the others nearly empty. To avoid this collapse, we exploit a physical property of the endmembers: each is selected at an angle where its corresponding target dominates, so its center peak intensity $c_k$ is approximately proportional to the total energy contributed by that target in the mixed speckle. Under the linear mixture model, the mixture coefficients for the total autocorrelation should therefore be proportional to $c_k$.

We encode this prior through an energy constraint. Let $c_k$ be the center pixel value of $\boldsymbol{x}_k$, and $r_k = c_k / \min_j c_j$ be the relative energy ratio. The expected mixing proportions are captured by a diagonal matrix $H_{\text{ideal}} = \mathrm{diag}(r_1, \ldots, r_N) / \sum_k r_k$. We then construct a weight matrix $M$ of the same dimensions as $X$, where each column $k$ is a constant vector whose entries equal the $k$-th diagonal element of $H_{\text{ideal}}$. Intuitively, $M$ encodes the prior that a pixel in the mixture should be represented by the $N$ endmembers according to the energy ratios observed at their center peaks.

The NMF objective is modified to a weighted reconstruction loss:

$$\min_{W,H \geq 0} \|M \odot (X - WH)\|_F^2 \tag{12}$$

where $\odot$ denotes element-wise multiplication, and $\|\cdot\|_F$ denotes the Frobenius norm. This loss penalizes deviations from the expected energy allocation more heavily, thereby preventing any single component from dominating the decomposition. The minimization is carried out via multiplicative update rules:

$$\begin{aligned} H_{kj} &\leftarrow H_{kj} \odot \frac{\left(W^T(M \odot X)\right)_{kj}}{(W^T(M \odot WH))_{kj} + \varepsilon} \\ W_{ik} &\leftarrow W_{ik} \odot \frac{\left((M \odot X)H^T\right)_{ik}}{(M \odot (WH))H^T_{ik} + \varepsilon} \end{aligned} \tag{13}$$

Finally, the reconstruction of each target from its separated autocorrelation is carried out based on the Wiener–Khinchin theorem [42]. The theorem states that for a real signal $s_i(\mathbf{r})$, its autocorrelation forms a Fourier transform pair with its power spectral density:

$$\mathcal{F}\{[s_i \star s_i](\mathbf{r})\} = |\mathcal{F}\{s_i\}|^2. \tag{14}$$

Applying the convolution model in Equation (1) and the linearity of the Fourier transform, the autocorrelation of the separated speckle component is dominated by the target's own autocorrelation, since the cross-correlations among targets are suppressed by the unmixing process. Consequently, the Fourier magnitude of the $i$-th target can be approximated by

$$|\mathcal{F}\{O_i\}| \approx \sqrt{\mathcal{F}\{[s_i \star s_i]\}}. \tag{15}$$

With the Fourier magnitude of each target recovered from its separated autocorrelation via the Wiener–Khinchin theorem, the missing phase information is retrieved using a Fienup-type phase retrieval algorithm [39]. The algorithm iteratively enforces constraints in both the spatial and Fourier domains. Starting from a random phase guess, the Fourier magnitude of each target is combined with the current phase estimate. An inverse Fourier transform is then applied, and the resulting spatial-domain estimate is constrained by a support region and non-negativity. The updated estimate is then transformed back to the Fourier domain, where the known Fourier magnitude is reimposed while the phase is retained. This process is repeated with a step size of 0.04 for four iterations to obtain the final reconstruction. The step size controls the rate of convergence and is set to a conservative value to avoid oscillation artifacts in the presence of noise and imperfect autocorrelation separation.

## 3. Experiment

### *3.1. Experimental Setup*

To verify the effectiveness of the proposed method, a red incoherent light source (M625L3, Thorlabs, Newton, NJ, USA) was employed for illumination. Multiple transparent targets, each measuring $0.5 \times 0.6$ mm, were arranged on the object plane with center-to-center separations exceeding the lateral optical memory effect (OME) range of the diffuser. This ensured that the speckle patterns originating from different targets were mutually uncorrelated. To impart a distinct linear polarization signature to each target, a polarizer (Daheng Optics, Beijing, China) with a specific orientation was placed immediately behind the corresponding target. A 220-grit ground glass diffuser(Edmund Optics, Barrington, NJ, USA), serving as the scattering medium, was positioned 360 mm behind the target plane. A camera (PCO.edge 4.2, pixel size 6.5 μm, PCO AG, Kelheim, Germany) was placed 120 mm behind the diffuser to record the speckle intensity patterns. A rotatable analyzer polarizer mounted directly in front of the camera was sequentially set to $0^\circ$, $45^\circ$, $90^\circ$, and $135^\circ$ to acquire four polarization-resolved speckle images. All data processing and image reconstruction were performed using MATLAB R2023b.

The lateral OME range of the scattering medium was characterized by measuring the speckle correlation decay as a point source was translated across the object plane. A 100 μm pinhole back-illuminated by a mounted LED (central wavelength 625 nm) served as the point source. The pinhole was translated laterally and a speckle pattern was recorded by the camera at each position, without the analyzer in the optical path. For each displacement, the normalized cross-correlation coefficient between the acquired speckle and a reference speckle taken at the initial position was computed. The lateral OME range was defined as the displacement at which this correlation coefficient decreased to one half of its maximum value. Under the present experimental configuration (object distance 360 mm, image distance 120 mm), the measured OME range of the 220-grit ground glass diffuser was 3.0 mm, as shown in Figure 3e. This value is substantially smaller than the inter-target separations adopted in the subsequent imaging experiments, confirming that the targets were located in mutually uncorrelated OME regions.

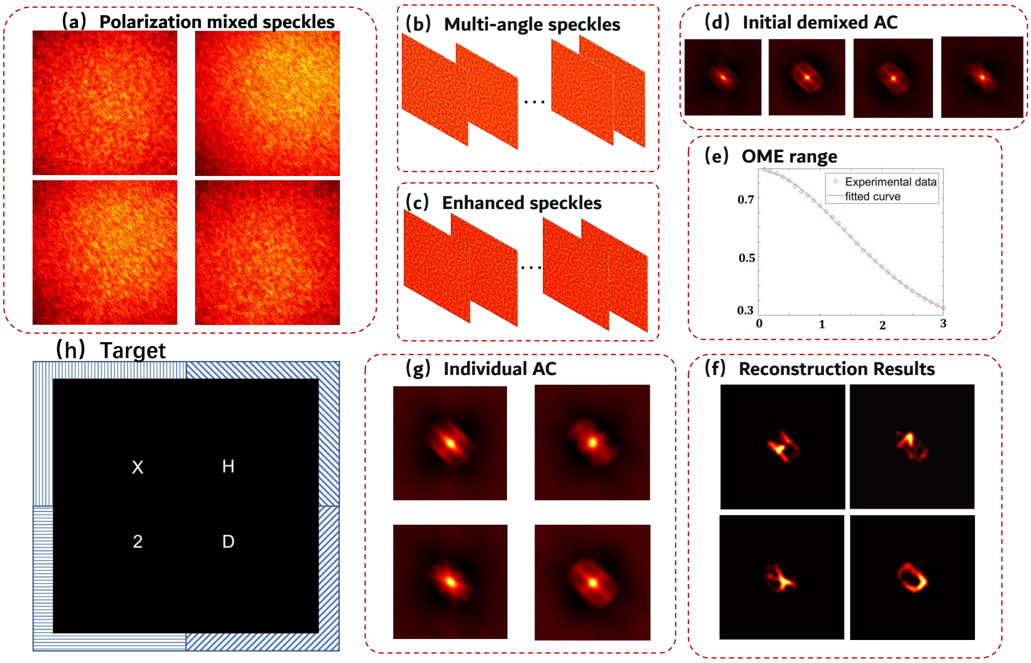


**Figure 3.** Experimental demonstration of multi-target imaging through scattering media. (**a**) Four polarization speckle images acquired at 0°, 45°, 90°, and 135°. (**b**) Multi-angle polarization speckle patterns synthesized from the Stokes parameters. (**c**) Enhanced speckle patterns after log-domain NLM filtering. (**d**) Endmember autocorrelations selected via ZNCC analysis. (**e**) Measured OME correlation curve of the ground glass diffuser. (**f**) Reconstructed target images obtained by phase retrieval from the separated autocorrelations. (**g**) Individual target autocorrelations decomposed by the energy-constrained NMF. (**h**) Binary target board.

### *3.2. Multi-Target Imaging Through Scattering Media*

The experimental system was constructed following the setup described in Section 3.1. A binary target board composed of four characters "2", "D", "X", and "H" was placed on the object plane, as shown in Figure 3h. Each target measured $0.5 \times 0.6$ mm and was covered by a polarizing film oriented at 0°, 45°, 90°, and 135°, respectively. The center-to-center spacing between adjacent targets was 5.5 mm, corresponding to approximately 1.8 times the lateral OME range.

The incident light, consisting of four target beams, passed through the ground glass diffuser, and a rotating polarizer was placed before the camera to acquire four polarization-resolved speckle images at 0°, 45°, 90°, and 135°, as shown in Figure 3a. From these four acquired images, multi-angle virtual polarization speckle patterns were synthesized via the Stokes parameters (see Figure 3b). A log-domain NLM filter was subsequently applied to all synthesized speckle images to enhance weak-target signatures (Figure 3c). After estimating the number of targets through local peak detection, structurally distinct endmember autocorrelations were selected via ZNCC analysis in the autocorrelation domain, serving as the initial input for the subsequent NMF, as depicted in Figure 3d. The decomposed individual target autocorrelations are shown in Figure 3g. Finally, phase retrieval was performed on each separated autocorrelation using the Fienup-type algorithm described in Section 2.2 to reconstruct the spatial structure of the corresponding target (see Figure 3f).

The structural details of all four targets are clearly recovered, demonstrating that the proposed method possesses robust reconstruction capability for targets with distinct polarization angles, and offers a promising avenue for advancing multi-target imaging theory through scattering media.

### 3.3. Robustness Validation Under Different Imaging Conditions

To further evaluate the robustness of the proposed method, we examined its imaging performance with respect to target separations beyond the OME range and polarization angle separations between targets.

To validate the imaging capability of the proposed method across different OME ranges, the experimental setup was kept unchanged while the target configuration was modified. The object plane consisted of four characters “2”, “7”, “X”, and “H”. The center-to-center spacing between targets “2” and “7”, as well as between “X” and “H”, was set to 8.5 mm, corresponding to 2.6 times the OME range, while the distances between “2” and “H” and between “7” and “X” were 6.5 mm, equivalent to 2.1 times the OME range, as illustrated in Figure 4(b1). The individual target autocorrelations obtained by the proposed method are shown in Figure 4(b2), and the corresponding reconstructed results are presented in Figure 4(b3). Compared with the reconstruction at 1.8 times the OME range, the proposed method effectively recovers the target information at both larger target separations. It is worth noting that, due to the limited divergence angle of the illumination source, the targets at the 2.6 $\times$ 2.1 OME configuration were near the edge of the effective illumination area. With parallel illumination covering a broader field, the proposed method is expected to extend to even higher OME multiples for imaging.

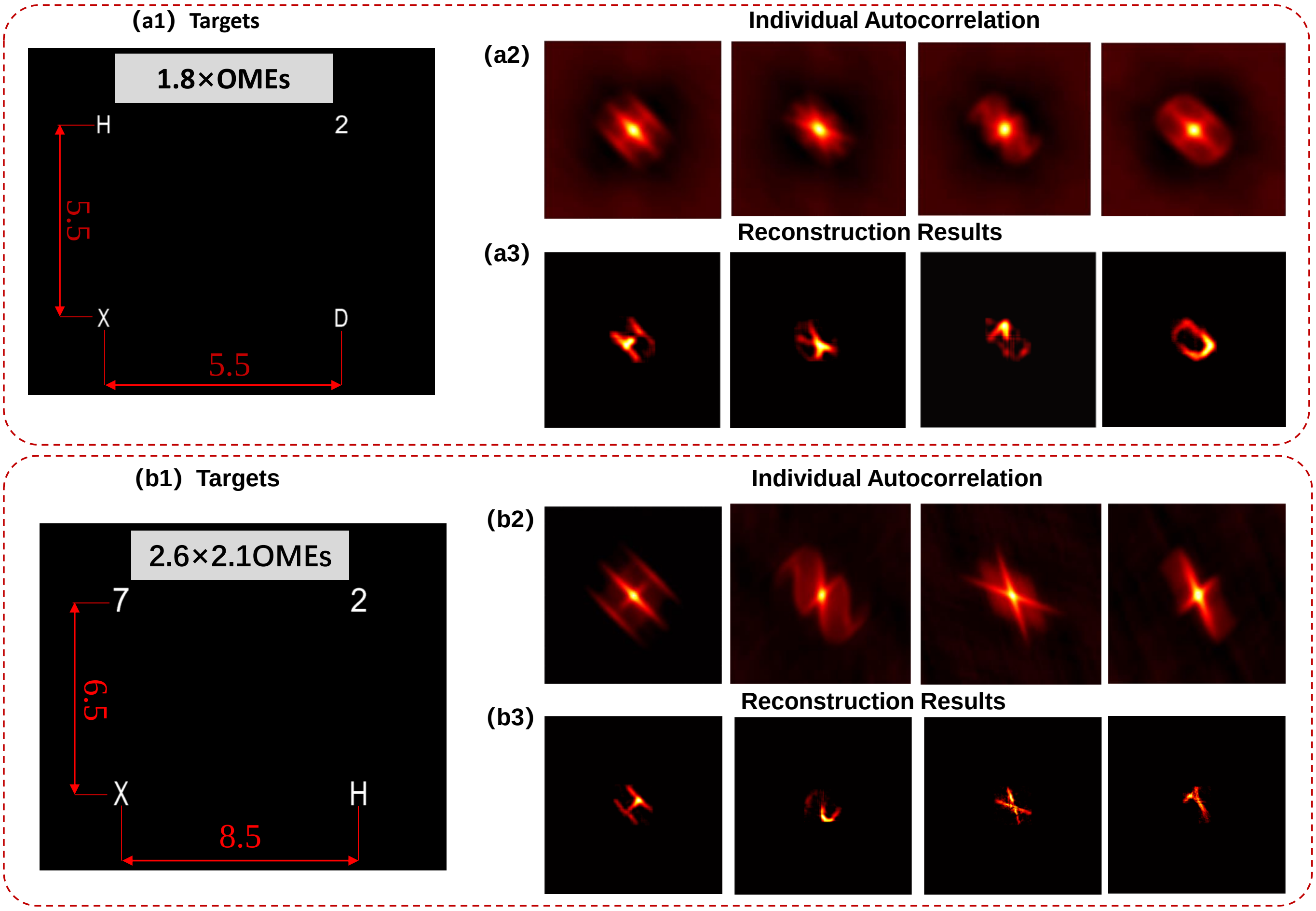


**Figure 4.** Comparative imaging results under different OME conditions. (**a1**–**a3**) Target configuration at 1.8 times the OME range, the corresponding individual target auto-correlations, and reconstructed target images. (**b1**–**b3**) Target configuration with increased separations, the corresponding autocorrelations and reconstructed target images.

To investigate the sensitivity of the proposed method to the polarization angle difference between targets, a second experiment was conducted using dual-target configurations with systematically varied polarization angle separations. Two transparent targets, each measuring 0.5 × 0.6 mm, were placed at a fixed spatial separation of 10 mm on the object plane, corresponding to 3.3 times the OME range. The targets were assigned polarization angles with a relative difference $\Delta\theta$ ranging from 10° to 90° in steps of 20°. For each configuration, four polarization-analyzed speckle images were acquired and processed through the proposed pipeline. The reconstructed target images for all tested polarization angle separations are presented in Figure 5, where clear target structures can be observed across the entire range from 10° to 90°. The average peak signal-to-noise ratio (PSNR) of the reconstructed dual-target pairs increased from 21.98 dB at $\Delta\theta = 10°$ to 26.03 dB at $\Delta\theta = 90°$, demonstrating that the reconstruction quality improves as the polarization angle separation increases. This trend is consistent with the physical expectation that larger polarization differences provide more distinct modulation coefficients for the two targets, thereby facilitating more effective blind separation. Notably, even at the smallest separation of 10°, the two targets remain distinguishable, indicating that the proposed method maintains reliable imaging performance under relatively challenging polarization contrast conditions. These results confirm the robustness of the polarization-guided unmixing framework with respect to the degree of polarization diversity among targets.

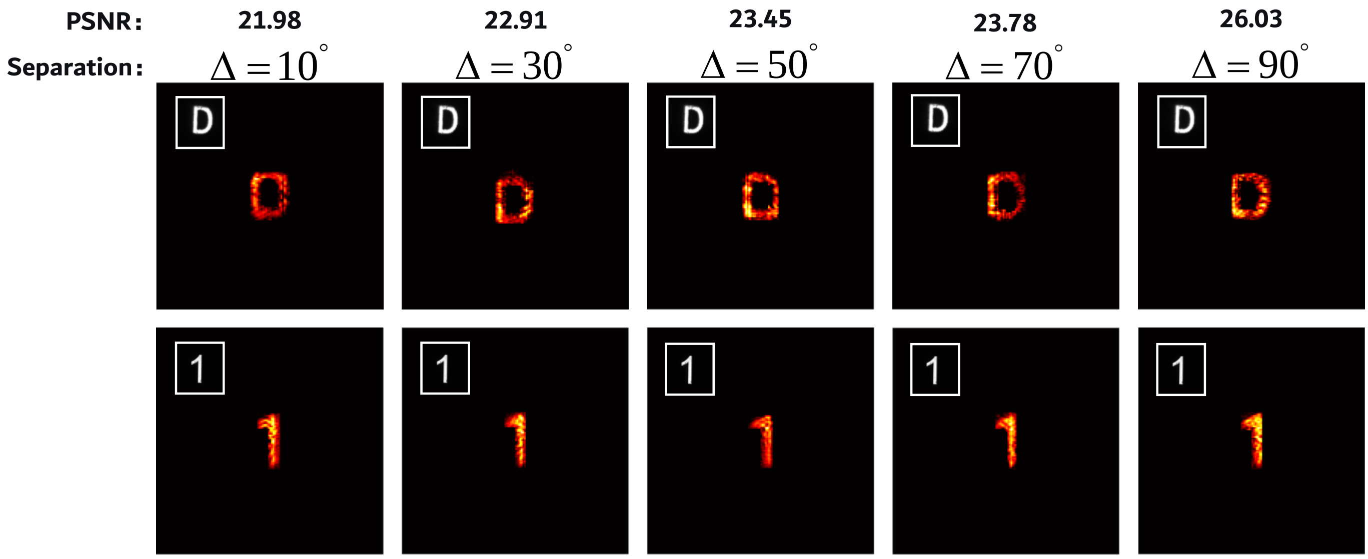


**Figure 5.** Reconstruction results for dual targets with varying polarization angle separations. The PSNR values represent the averaged data for dual-object reconstructions with references.

*3.4. Imaging Performance with Varying Target Counts*

To further demonstrate the robustness and feasibility of the proposed method across different target counts, the experimental setup was kept unchangedwhile the number of targets was progressively increased from two to five. The polarization angles were 0° and 90° for the two-target case, 0°, 45°, and 90° for the three-target case, 0°, 45°, 90°, and 135° for the four-target case, and 0°, 36°, 72°, 108°, and 144° for the five-target case. The comparative results are presented in Figure 6. Effective imaging beyond the OME range was achieved for all tested target numbers, with the lowest reconstructed PSNR remaining at 25 dB, confirming that the proposed method can reliably resolve the structural information of individual targets regardless of their number.

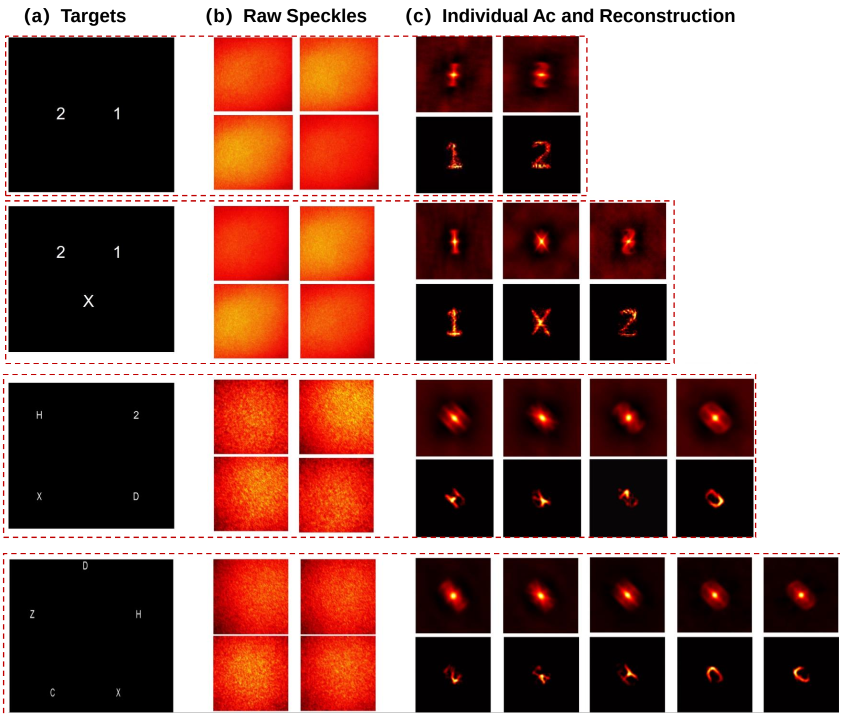


**Figure 6.** Reconstructed images for target numbers ranging from two to five.Reconstructed images for target numbers ranging from two to five. Columns (**a**) and (**b**) show the ground truth target configurations and the corresponding raw captured speckle patterns for each target count, respectively. Column (**c**) show the separated individual target autocorrelations and the corresponding reconstructed target images, respectively. Rows from top to bottom correspond to two-, three-, four-, and five-target cases, respectively.

## 4. Conclusions and Discussion

This article presented a polarized blind unmixing framework that enables multi-target imaging through scattering media beyond the OME range. Experimental results demonstrate that the proposed method successfully resolves multiple targets with distinct polarization angles at separations from 1.8 to 2.6 times the OME range, with PSNR values above 25 dB for target counts from two to five.

The imaging performance is constrained by the illumination coverage and the polarization-maintaining property of the scattering medium. The method has been validated up to 2.6 times the OME range, and this boundary can be extended with collimated illumination. For partially depolarizing media, the distinct polarization responses among targets may become degraded.

The current implementation relies on incoherent LED illumination to ensure intensity-domain linear superposition, which is essential for our mixture model. Extension to coherent laser illumination would offer higher brightness but would introduce cross-interference between speckle fields and enhanced coherent speckle noise, requiring coherence control or modulation-based detection schemes in future work.

The achievable imaging range can be further extended with improved camera detection capabilities. The method requires no prior knowledge or active modulation, ensuring noninvasive detection and holding potential for single-frame imaging when combined with polarization-sensitive detectors. For more complex scenarios involving multiple targets or continuously varying samples, additional constraints such as spatial priors, temporal modulation, or wavelength diversity can be incorporated.

With the adoption of a high-quantum-efficiency polarization camera, the proposed framework is expected to realize single-shot multi-target imaging beyond the OME range.

This work establishes a practical pathway for extending speckle-correlation imaging to multiple targets in distinct OME regions.

**Author Contributions:** Conceptualization, J.D., X.D., P.H. and F.L.; methodology, J.D.; software, J.D., T.Z. and P.H.; validation, J.D.; formal analysis, J.D., T.Z. and X.D.; investigation, J.D. and T.Z.; resources, F.L.; data curation, F.L.; writing—original draft preparation, J.D.; writing—review and editing, J.D. and T.Z.; visualization, J.D.; supervision, T.Z., X.D., P.H. and F.L.; project administration, F.L.; funding acquisition, F.L. All authors have read and agreed to the published version of the manuscript.

**Funding:** This research was funded by the National Natural Science Foundation of China (62405231, 62405235, 62575229), Beijing Key Laboratory of Advanced Optical Remote Sensing Technology (AORS202405), China Postdoctoral Science Foundation (2024M762527), Shaanxi Province High-level Innovation and Entrepreneurship Talent Program (H02439005), and Natural Science Foundation of Shaanxi (S2024-JC-JCQN-60, S2025-JC-QYTS-0107, 2025JC-QYCX-05).

**Data Availability Statement:** Data underlying the results presented in this paper are not publicly available at this time but may be obtained from the authors upon reasonable request.

**Conflicts of Interest:** The authors declare no conflicts of interest.

## References

1. Vellekoop, I.M.; Mosk, A.P. Focusing coherent light through opaque strongly scattering media. *Opt. Lett.* **2007**, *32*, 2309. [CrossRef] [PubMed]
2. Liu, J.; Feng, Y.; Wang, Y.; Liu, J.; Zhou, F.; Xiang, W.; Zhang, Y.; Yang, H.; Cai, C.; Liu, F.; et al. Future-proof imaging: Computational imaging. *Adv. Imaging* **2024**, *1*, 012001. [CrossRef]
3. Luo, X.; Wang, S.; Liu, J.; Dong, X.; He, P.; Yang, Q.; Chen, X.; Zhou, F.; Zhang, T.; Feng, S.; et al. Revolutionizing optical imaging: Computational imaging via deep learning. *Photonics Insights* **2025**, *4*, R03. [CrossRef]
4. Freund, I.; Rosenbluh, M.; Feng, S. Memory effects in propagation of optical waves through disordered media. *Phys. Rev. Lett.* **1988**, *61*, 2328–2331. [CrossRef] [PubMed]
5. Judkewitz, B.; Horstmeyer, R.; Vellekoop, I.M.; Papadopoulos, I.N.; Yang, C. Translation correlations in anisotropically scattering media. *Nat. Phys.* **2015**, *11*, 684–689. [CrossRef]
6. Mosk, A.P.; Lagendijk, A.; Lerosey, G.; Fink, M. Controlling waves in space and time for imaging and focusing in complex media. *Nat. Photonics* **2012**, *6*, 283–292. [CrossRef]
7. Cui, M. A high speed wavefront determination method based on spatial frequency modulations for focusing light through random scattering media. *Opt. Express* **2011**, *19*, 2989–2995. [CrossRef] [PubMed]
8. Popoff, S.M.; Lerosey, G.; Carminati, R.; Fink, M.; Boccara, A.C.; Gigan, S. Measuring the Transmission Matrix in Optics: An Approach to the Study and Control of Light Propagation in Disordered Media. *Phys. Rev. Lett.* **2010**, *104*, 100601. [CrossRef] [PubMed]
9. Popoff, S.M.; Lerosey, G.; Fink, M.; Boccara, A.C.; Gigan, S. Controlling light through optical disordered media: Transmission matrix approach. *New J. Phys.* **2011**, *13*, 123021. [CrossRef]
10. Xu, X.; Xie, X.; He, H.; Zhuang, H.; Zhou, J.; Thendiyammal, A.; Mosk, A.P. Imaging objects through scattering layers and around corners by retrieval of the scattered point spread function. *Opt. Express* **2017**, *25*, 32829–32840. [CrossRef]
11. Katz, O.; Heidmann, P.; Fink, M.; Gigan, S. Non-invasive single-shot imaging through scattering layers and around corners via speckle correlations. *Nat. Photonics* **2014**, *8*, 784–790. [CrossRef]
12. Osnabrugge, G.; Horstmeyer, R.; Papadopoulos, I.N.; Judkewitz, B.; Vellekoop, I.M. Generalized optical memory effect. *Optica* **2017**, *4*, 886–892. [CrossRef]
13. Luo, X.; Liu, J.; Wang, X.; Li, J.; Xiang, M.; Wang, D.; Duan, J.; Zhang, T.; Dong, X.; Geng, Z.; et al. Single-shot scattering imaging beyond the optical memory effect via speckle-sparsity decoupling. *Adv. Photonics* **2026**, *8*, 036009. [CrossRef]
14. Tang, D.; Sahoo, S.K.; Tran, V.; Dang, C. Single-shot large field of view imaging with scattering media by spatial demultiplexing. *Appl. Opt.* **2018**, *57*, 7533–7538. [CrossRef] [PubMed]
15. Guo, C.; Liu, J.; Li, W.; Wu, T.; Zhu, L.; Wang, J.; Wang, G.; Shao, X. Imaging through scattering layers exceeding memory effect range by exploiting prior information. *Opt. Commun.* **2019**, *434*, 203–208. [CrossRef]
16. Zhang, J.; Jing, Z.; Zhao, S.; Wang, X.; Ma, G.; Wang, Y.; Zhao, Y.; Liu, R.; Li, F. Multi-target object scattering imaging with intensity correlation of structured illumination. *Opt. Lett.* **2023**, *48*, 1486–1489. [CrossRef] [PubMed]

17. Li, L.; He, Q.; Wang, Y.; Liu, H.; Zhuang, L.; Chen, Z. Imaging through scattering layers exceeding memory effect range with spatial-correlation-achieved point-spread-function. *Opt. Lett.* **2018**, *43*, 1670–1673. [CrossRef] [PubMed]
18. Guo, E.; Zhu, S.; Sun, Y.; Bai, L.; Zuo, C.; Han, J. Learning-based method to reconstruct complex targets through scattering medium beyond the memory effect. *Opt. Express* **2020**, *28*, 2433–2446. [CrossRef] [PubMed]
19. Zhou, M.; Bai, C.; Zhang, Y.; Li, R.; Peng, T.; Qian, J.; Dan, D.; Min, J.; Zhou, X. Deep-Learning-Based Rapid Imaging Through Scattering Media Beyond the Memory Effect. *IEEE Photonics Technol. Lett.* **2022**, *34*, 295–298. [CrossRef]
20. Zhou, M.; Bai, C.; Zhang, Y.; Li, R.; Peng, T.; Qian, J.; Dan, D.; Min, J.; Zhou, X.; Yao, B. Diffusion model-based imaging through scattering media beyond the memory effect. *Opt. Lett.* **2023**, *48*, 5305–5308.
21. Wang, X.; Li, J. Physics-informed deep learning for scattering imaging beyond the optical memory effect. *Opt. Express* **2024**, *32*, 1234–1245.
22. Chen, Y.; Zhang, H.; Liu, J.; Wang, S.; Li, X. Adaptive optics-enhanced wide-field imaging through dynamic scattering media. *Adv. Photonics* **2023**, *8*, 056001.
23. Lu, D.; Chen, J.; Tian, Y.; Cai, J.; Chen, Z.; Peng, X.; He, W. Customizing the field of view for imaging through scattering media. *Adv. Photonics Nexus* **2025**, *4*, 066004. [CrossRef]
24. Tang, C.; Wang, F.; Tang, Z.; Chu, Y.; Situ, G. TransFNet: A physics-enhanced transformer for speckle correlation imaging. *Opt. Commun.* **2025**, *591*, 132126. [CrossRef]
25. Wei, Y.; Lu, D.; Liao, M.; He, W.; Peng, X. Noninvasive imaging of two isolated objects through a thin scattering medium beyond the 3D optical memory effect. *Opt. Express* **2021**, *29*, 18807–18816. [CrossRef] [PubMed]
26. Wang, X.; Jin, X.; Li, J.; Lian, X.; Ji, X.; Dai, Q. Prior-information-free single-shot scattering imaging beyond the memory effect. *Opt. Lett.* **2019**, *44*, 1423–1426. [CrossRef] [PubMed]
27. Li, W.; Liu, J.; He, S.; Liu, L.; Shao, X. Multitarget imaging through scattering media beyond the 3D optical memory effect. *Opt. Lett.* **2020**, *45*, 2692–2695. [CrossRef] [PubMed]
28. Wang, X.; Jin, X.; Li, J. Blind position detection for large field-of-view scattering imaging. *Photonics Res.* **2020**, *8*, 920. [CrossRef]
29. Wei, Y.; Guo, E.; Zhao, Y.; Mu, D.; Bai, L.; Han, J. Prior-free mixed speckle simplex separation strategy for multi-object imaging through thin scattering media beyond the optical memory effect. *APL Photonics* **2023**, *8*, 126108. [CrossRef]
30. Collett, E. *Field Guide to Polarization*; SPIE Press: Bellingham, WA, USA, 2005.
31. Chipman, R.A.; Lam, W.S.; Young, G. *Polarized Light and Optical Systems*; CRC Press: Boca Raton, FL, USA, 2018.
32. Azzam, R.M.A. Stokes-vector and Mueller-matrix polarimetry. *Opt. Lett.* **1996**, *33*, 1396–1408.
33. Schechner, Y.Y.; Narasimhan, S.G.; Nayar, S.K. Polarization-based vision through haze. *Appl. Opt.* **2003**, *42*, 511–525. [CrossRef] [PubMed]
34. Li, X.; Han, Y.; Wang, H.; Liu, T.; Chen, S.C.; Hu, H. Polarimetric Imaging Through Scattering Media: A Review. *Front. Phys.* **2022**, *10*, 815296. [CrossRef]
35. Shen, L.; Zhang, L.; Qi, P.; Zhang, X.; Li, X.; Huang, Y.; Zhao, Y.; Hu, H. Polarimetric binocular three-dimensional imaging in turbid water with multi-feature self-supervised learning. *PhotoniX* **2025**, *6*, 24. [CrossRef]
36. Yang, K.; Liu, F.; Liang, S.; Xiang, M.; Han, P.; Liu, J.; Dong, X.; Wei, Y.; Wang, B.; Shimizu, K.; et al. Data-driven polarimetric imaging: A review. *Opto-Electron. Sci.* **2024**, *3*, 230042. [CrossRef]
37. Luo, X.; Wang, X.; Han, P.; Liu, J.; Liu, Y.; Zhang, T.; Liu, F. Polarization-guided three-dimensional recovery through scattering media. *Opt. Lett.* **2026**, *51*, 1235–1238. [CrossRef] [PubMed]
38. Duan, J.; Liu, J.; Li, C.; Han, P.; Liu, F. Noninvasive scattering imaging beyond the 3D optical memory effect based on the linear polarization characteristics. *Opt. Lasers Eng.* **2026**, *205*, 109916. [CrossRef]
39. Fienup, J.R. Phase retrieval algorithms: A personal tour [Invited]. *Appl. Opt.* **2013**, *52*, 45–56. [PubMed]
40. Wang, K.; Song, L.; Wang, C.; Ren, Z.; Zhao, G.; Dou, J.; Di, J.; Barbastathis, G.; Zhou, R.; Zhao, J.; et al. On the use of deep learning for phase recovery. *Light. Sci. Appl.* **2024**, *13*, 190–235. [CrossRef] [PubMed]
41. Wei, J.; Li, R.; Wu, J.; Zhang, Q.; Gao, Y.; Cao, L. Development and Application of Phase Retrieval Wavefront Reconstruction Techniques (Invited). *Laser Optoelectron. Prog.* **2024**, *61*, 0211001.
42. Leibovich, N.; Barkai, E. Aging Wiener-Khinchin Theorem. *Phys. Rev. Lett.* **2015**, *115*, 080602. [CrossRef] [PubMed]